applied sciences

MDPI

Article

Numerical Simulation on Corneal Surface Behavior Applying Luminous Beam Levels

Fernando Guevara-Leon [1], Mario Alberto Grave-Capistrán [1], Juan Alejandro Flores-Campos [2], Jose Luis Torres-Ariza [1], Elliot Alonso Alcántara-Arreola [1] and Christopher René Torres-SanMiguel [1,*]

[1] Instituto Politécnico Nacional, Escuela Superior de Ingeniería Mecánica y Eléctrica, Sección de Estudios de Posgrado e Investigación, Unidad Zacatenco, Ciudad de México 07738, Mexico; jtorresa1302@alumno.ipn.mx (J.L.T.-A.)

[2] Instituto Politécnico Nacional, Unidad Profesional Interdisciplinaria en Ingeniería y Tecnologías Avanzadas, Ciudad de México 07340, Mexico

* Correspondence: ctorress@ipn.mx; Tel.: +52-555-729-600 (ext. 54815)

Abstract: According to the World Health Organization (WHO), approximately 1.3 billion people experience visual impairments. Daily exposure to various levels of luminous beams directly impacts the front layer of the visible structure, leading to corneal injuries. To comprehensively understand this, we reconstructed a three-dimensional model utilizing the PENTACAM® system. This enabled us to accurately determine the 50th percentile dimensions of the fibrous layer of the eyeball. Using the Ogden mathematical model, we developed a 3D cornea model, treating it as a soft tissue with predictable behavior, considering mechanical properties such as viscoelasticity, anisotropy, and nonlinearity. Employing the Finite Element Method (FEM), we analyzed five distinct test scenarios to explore the structural response of the cornea. Luminous beam properties were instrumental in establishing varying mechanical loads, leading to structural deformations on the corneal surface. Our findings reveal that when a smartphone's screen emits light at a frequency of 651.72 THz from 200 mm, displacements in the corneal layer can reach up to 9.07 µm. The total load, computed by the number of photons, amounts to 7172.637 Pa.

Keywords: biomechanics; cornea; displacements; luminous beams; structural deformation

Citation: Guevara-Leon, F.; Grave-Capistrán, M.A.; Flores-Campos, J.A.; Torres-Ariza, J.L.; Alcántara-Arreola, E.A.; Torres-SanMiguel, C.R. Numerical Simulation on Corneal Surface Behavior Applying Luminous Beam Levels. *Appl. Sci.* **2023**, *13*, 12132. https://doi.org/10.3390/app132212132

Academic Editors: Velia D'Agata and Grazia Maugeri

Received: 21 September 2023
Revised: 31 October 2023
Accepted: 3 November 2023
Published: 8 November 2023

1. Introduction

In Mexico, visual disease cases number around 7.1 million, and based on a study by Instituto Nacional de Estadística y Geografía (INEGI), 33% have visual impairment or blindness. These diseases affect people who are 50 years old to elderly and are often due to long periods of luminescence exposure from high-level irradiation sources toward the ocular organs [1–3].

The first model of the eye that used the Finite Element Method (FEM) was from around 1997. This model was made based on empirical values according to the anatomy of the human eye. The prediction of optical image quality at various levels of defocus aided this study with refractive surgical methods, such as photorefractive keratectomy and automated lamellar keratoplasty [4]. In 2002, in Germany, experiments in two locations with different values of UV and UVB radiation (305 nm and 315 nm) demonstrated that several instances of damage appeared in areas with higher ambient radiation [5]. In 2006 in Singapore, a 2D finite element-based model was designed as a thermal model for early detection of disease, and research revealed the effectiveness against the infrared method (0.33% error) and the FEM model (0.127 error) [6]. In 2010, a mathematical model was performed applying a variant of the FEM (sigma) to increase the accuracy of bioheat transfer due to experimental treatments by the method of immunotherapy against cancerous tumors in the eye. By using the hyperthermia method, the tumor temperature can be raised without affecting its properties [7]. In 2012, an implant was developed to treat glaucoma; the cornea model

(located for transplantation) was used under specific conditions, and the simulation was performed based on the temperature variant and its prevention in the implant [8].

In 2015, Salesian Polytechnic University developed an ocular model of the human eye as a tool for intraocular pressure measurement for patients requiring glaucoma prevention. The cornea thickness was used to obtain a mathematical model to determine the severity of the disease in patients [9]. Similarly, in 2015, a model of the human organ was announced; this one was performed to study primary eye blast injury, calculating the stresses around it. Considering the eye's shape, it is possible to produce a resonance effect, increasing the damage, considering the loading conditions in different lengths from the blast and the explosive mass loading (trinitrotoluene) [10]. A numerical simulation by I. Simonini and A. Pandolfi aims to analyze the mechanical properties in the cornea post-surgery. It is used for visual correction in patients with eye diseases. The numerical models provide quantitative and accurate information about the refractive properties in the cornea [11]. In 2016, a FEM model of the human eye was generated, allowing daily evaluation of the optic nerve motion [12].

In Iran in 2016, a numerical analysis of the whole eyeball (cornea, aqueous humor, iris, ciliary body, crystalline lens, vitreous humor, retina, sclera, optic nerve, and external eye muscles) under loads that are created by trinitrotoluene was performed. This analysis was performed through a Lagrangian model and a Eulerian computational method [13]. In 2016, an analysis of the damage caused by a tennis ball at 69 m/s hitting a human eye (ex vivo) was performed. The study defines the stresses and deformations in the main parts of the eyeball, which, including the cornea, by magnetic resonance imaging results exhibit displacements of up to 0.045 µm and stress of 8.27 MPa [14]. In the same year, by Whitford, C. et al., an in vivo cycle method in a porcine eye was developed to determine the variation of the mechanical behavior of the ocular surface (sclera). The methodology proposes an analysis of the sclera, measuring the internal displacements generated through digital cameras and image correlation software [15]. Computational models were made using topographic data of 10 patients who suffered refractive grid extraction due to astigmatism or myopia. Finite element analysis was performed based on intraocular pressure; a study of intraocular forward pressure estimates the corneal displacement when the extraction procedure is carried out. Intraocular approaches reveal less impact on collagen layers [16]. In 2018, an eye model was developed to analyze the stress generated by intraocular pressure; the model focuses on a correlation between eyes with and without glaucoma, which tend to stiffness. The aim is to estimate the pathophysiology of glaucoma by identifying possible risk factors [17]. In 2023, biological tissue in a finite element model was developed, taking into consideration type of mesh, mechanical properties and compressive loads. The aim was to remodel the soft tissue of the liver under a pathogenesis, considering hyperelasticity and viscoelasticity as main properties for the numerical solution to analyze the structural behavior; results show an approach of the deformations through a fractal method in the surface of the liver [18].

Research by M. Xu focused on corneal biomechanical and optical behavior, applying the FEM, and proposes a step-by-step methodology to reconstruct a model in the different parts and layers [19]. The primary considerations for realizing this numerical analysis are about the type of material. The visual organ is viscoelastic, considered a material capable of absorbing energy, deforming to its original state, and dissipating much of it [20]. In addition, the mechanical properties of its tissues, the human organ is said to be hyperelastic, anisotropic, and nonlinear due to its unique properties. Therefore, a mathematical model capable of satisfying the analysis, the Ogden model, was proposed to be used [21]. The focus of the work was to analyze the cornea and its damage. It is essential to consider the distinctive properties of the cornea for reliable analysis, such as elasticity, creep, relaxation, and hysteresis [22]. Before performing the investigation, it is essential to note that light must be considered from its purest part, an electromagnetic wave. The energy emitted by the photon is considered, using Planck's constant, the speed of light, and the wavelength of the emitter itself [23]. Ramirez, O. developed a methodology analyzing the behavior of tissues

and bones, replicating in an experimental test bench the movements of a rib of the human body in the breathing process; results show the characterization of the force and strain and the main considerations when parts of the human body are used under compressive stress [24]. Rezvan Fada investigated the mechanical properties of bone cement material without porosity to carry out a FEA analysis to study the structural stability and stress behavior in the material; outcomes allow the quantification of the porosity effect of the calcium phosphate to develop improvements while applying strontium nitrate [25].

This research aims to analyze the behavior in the eyeball's corneal surface when prolonged luminous beams irradiate it at a minimum distance. A three-dimensional model of the human visual organ is constructed, based on accurate dimensions from the PENTACAM® study, and supported by the clinical literature; through a numerical simulation, it is possible to establish the requirements to configure and represent the study cases of the biological material. The results show an approach quantifying the displacements on the corneal surface due to different light beams' exposition.

2. Materials and Methods

2.1. Three-Dimensional Model

The 3D modeling procedure considers the human eyeball and the main parts composing it. First, research was done on the accurate dimensions of the visual organ of the 50th global percentile [26]; then, the measurements were obtained with clinical reports and literature. Further, a 2D sketch was created to validate it and develop a 3D detailed design; finally, we created the numerical simulation considering the 3D model and the study cases. This research presents a complete 3D model of the human organ; it was considered a topographic study, and we obtained the values in Table 1.

Table 1. Dimensions of the specific parts of the human organ, 50th percentile.

Zone	Dimensions
Cornea	D: 10 mm. Volume: 57.5 mm^3. Thickness: 0.5 mm.
Sclera	Different thicknesses. Leaf blade: 0.8 mm. Equator: 0.4 mm. Optic nerve insertion: 4.5 mm.
Iris	D: 12.33 mm. Ang. iris–cornea = 56°. Iris–crystalline distance 1.8 mm. Corrugated.
Pupil	D: 3 mm. "Its diameter is between 3 and 4.5 millimeters in the human eye. It can widen to between 5 to 9 mm in the dark".
Crystalline	Three layers and greater curvature is the back face. Capsule thickness: 0.5 mm. Core: 2.1 mm.
Ciliary muscle/ciliary body	Thickness: 0.6 mm. Distance between the ciliary muscle and ciliary body: 0.35–0.3 mm.
Choroid	Thickness: 0.4 mm
Retina	Different thicknesses. Periphery: 2 mm, optic nerve insertion: 5 mm.
Pos/Ante Camera	Vol ante: 192 mm^3.
Eyelids/Corneal cavity	Different thicknesses. Leaf blade: 1 mm. Equator: 1.5 mm/sclera–cavity space: 0.1 mm. Thickness: 1.5 mm. "Their distances vary between 12–14.5 mm at their maximum opening, and 3.5 mm is considered the minimum".
Axial length	24.66 mm.

Based on the same study and the literature, considering the 2D sketch, a 3D model was developed on the computer program SolidWorks® 2022 by Dassault Systèmes, Velizy-Villacoublay (France). Since the eye is composed of two liquids (99% water), the vitreous and aqueous humor [27], in addition, the capsule of the lens is considered, and it is a vital element in the capability of the organ to collect external stimuli and its purpose as a barrier; it is divided into three parts: the lens capsule, the cortex of the lens, and the nucleus of the lens. It is essential to add these elements to the model because the current study of this research focuses on the analysis of light waves under the surface of the eyeball. The

thickness of the capsule was 0.5 mm, and the diameter of the nucleus was 2.1 mm; the study mainly considers the corneal behavior due to loads on the surface with luminous beams. Furthermore, it is important to consider these internal layers where the luminous lengths can breach them. Figure 1 shows a cross-section view of the eyeball reconstruction.

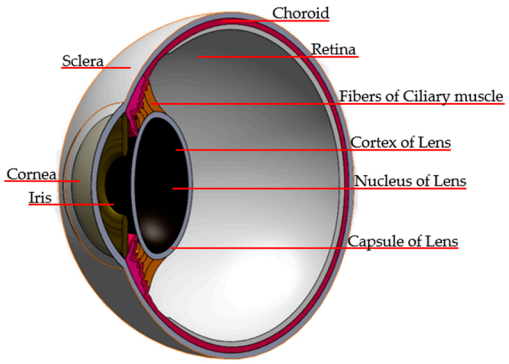

Figure 1. Reconstruction of a human eyeball and its parts; isometric cross-section view.

From the data shown in Table 1, it was possible to reconstruct a 3D model of the visual organ and apply specific mechanical properties for each part to develop the numerical analysis. In the model, the vitreous humor was removed to appreciate its features better, as shown in Figure 1.

2.2. Numerical Requirements

The eyeball is continuously under different beam levels of energy. Nowadays, every single person uses devices or tools that are sources of light and that emit luminous brightness, which can cause injuries or blindness. To develop the numerical simulation, it was necessary to consider the eyeball and the corneal surface where the luminous beams impact; different common cases were considered, such as sunlight, the screen of a smartphone, and beams of light from devices (e.g., high brightness luminaries or laser light); depending on the case, different compression loads are exerted on the structural surface. Once the detailed design was completed successfully, it was exported to a computer program where the pre-processing, numerical configuration, solution, and post-processing were carried out; the FEM was applied, high-order tetrahedral elements were considered to the whole model, and the irradiance of the light to the cornea was at a 200 mm distance. The model in Figure 2 shows a cross-section of the eyeball and one study case representation.

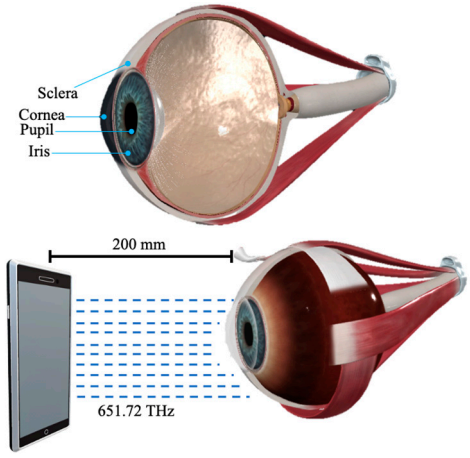

Figure 2. Anterior parts of the eyeball and the smartphone study case representation.

The developed model was considered for the numerical analysis. It is essential to follow the methodology proposed. After the reconstruction of the eyeball's 3D model, the

next step was to export the model in STL format to the computer program MATLAB®; in this program, a 3D scenario was created to perform the numerical solution. The model consists of 17,131 faces, with a weight of 587 kb. Then, a tetrahedral mesh was applied to the model, and high-order tetrahedral finite elements were applied. There are 10 nodes per element: 4 angular nodes (vertices) and 6 nodes between each vertex. Figure 3 shows the corneal surface (area to be analyzed) in tetrahedral elements.

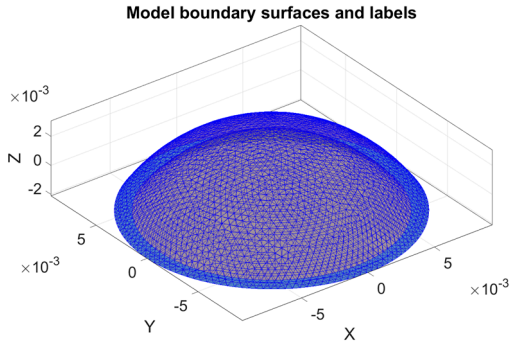

Figure 3. Tetrahedral mesh on the corneal surface.

This analysis only considers the corneal surface as the element of study, considering its mechanical properties, such as its percentage of transparency (70%) and convex shape. In the MATLAB® program student version, the boundary conditions were applied on specific nodes to fix the cornea's contour (474 points), and nodes of movement (2223 points) on the corneal surface were assigned to the study case. The structure of the cornea is composed of collagen fibers; the human cornea has the highest penetration compared to domestic animals such as rabbits or pigs. The modulus of elasticity in the human cornea is approximately 2.29 MPa with a variation of ±0.06 MPa (in ages from 18 to 30). Thus, the average is from 0.13 MPa to 0.43 MPa because the younger the person, the lower the value, while elderly people have higher values [28]. In the anterior part of the model, the cornea is considered as a deformable material, while the posterior parts of the visual organ were taken as anchorage elements to achieve the numerical simulation for this study; in Figure 4, the anchorage nodes and the movement nodes were configured in the whole model.

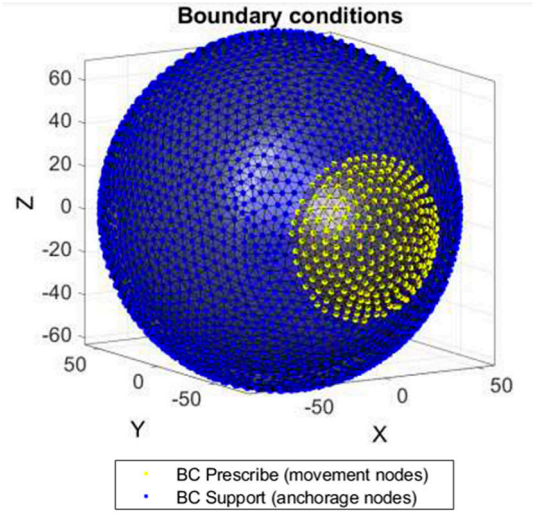

Figure 4. Boundary conditions are assigned on the model, blue dots as support nodes and yellow dots as movement nodes.

Models are used to describe mechanical behavior and obtain stress and strain patterns applied to organic tissues like the human cornea. The Ogden model is regarded as a

suitable model for hyperelastic material behavior and depicts strain energy $\boldsymbol{W}$ considering the main extensions: λ_1, λ_2, λ_3. The results of stress tests are obtained with an acceptable approximation using this mathematical model. The appropriate expression is:

$$\boldsymbol{W} = \sum_{p=1}^{n} \frac{u_p}{\alpha_p} \cdot \left(\lambda_1^{\alpha p} + \lambda_1^{\alpha p} + \lambda_1^{\alpha p} - 3 \right)$$

3. Results

3.1. Beam Type versus Incident Charge Ratio

To perform the proposed analysis, it was essential to consider the typical cases in which the types of light can be presented. They are differentiated by wavelength, and depending on this value, they were positioned in different electromagnetic spectra. The selected case studies were set as shown in Table 2; there were five daily cases with specific values of the wavelength, frequency, and types of radiation that matched the values raised, taken arbitrarily. The initial proposal included incident light beam charges, the charge of a photon, and the number of photons. The range of values in each case study has already been established in five specific cases developed from the principle of optical tweezers [29]. The power and wave frequency were predominant in load changes in the five cases that already had the application to obtain the total load in each case.

Table 2. Cases of study.

Case No.	Wavelength	Frequency	Electromagnetic Spectrum
1	300 nm	999.31 THz	UV-B
2	350 nm	856.55 THz	UV-A
3	460 nm	651.72 THz	Visible Spectrum (Blue)
4	1000 nm	299.79 THz	Near Infrared
5	1500 nm	199.86 THz	Medium Infrared

3.2. Model Validation

It was essential to validate the proposed model; the cornea is considered a regular geometry. Therefore, it is possible to view a proportional fraction to validate a specific area. Hence, 25% of the corneal surface was considered for the analysis. This was mainly to reduce the computational resources and the time to solve. Figure 5 shows a free-body diagram in different views.

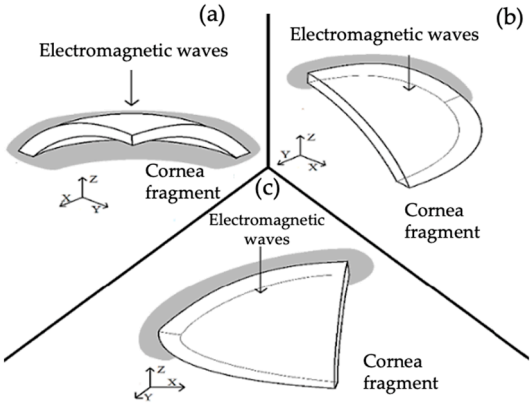

Figure 5. Free-body diagram, (**a**) base constraint, (**b**) lateral constraint, and (**c**) adjacent lateral constraint.

The boundary conditions had three constraints, shown in Figure 5, marked by a gray shadow; where it exists, they were applied in each of the three views of the figure. These conditions belonging to the nodes involved in the numerical analysis program are shown

in Figure 6. As a result of this validation, 26 nodes (blue dots) were assigned at the base of the corneal structure.

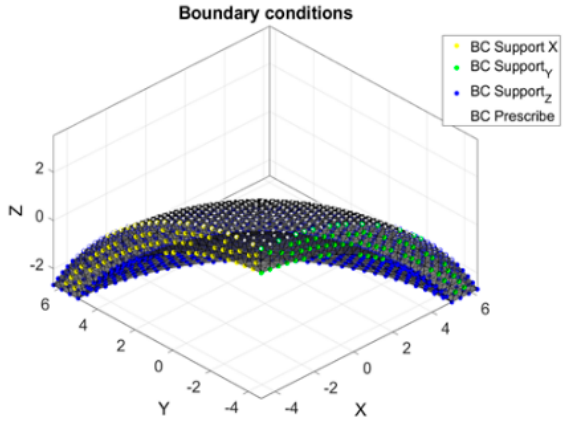

Figure 6. Corneal section; anchorage and movement node assignment.

Several researchers contemplated comparing the data from the necessary mechanical properties to be used. The following parameters were selected for a K (modulus of compressibility) of 100 μ, shear modulus of 0.282 MPa, and elastic modulus of collagen fibers (EFIB) of 38.950 MPa [30].

The values assigned were compared with an experimental investigation from 1972. In this specific case, the displacement carried out at the specific moment of the incidence of an amount of load, the whole process was quantifiable in an experiment with the corneas of 15 specimens of different persons [31]. The results of the comparison are shown in Table 3.

Table 3. Correlation of results.

Case	Load (mmHg)	Deformation (μm)	Experimental Values Range (μm)
1	10	10.7	1.7–11.8
2	15	17.989	9.59–18.4
3	20	23.1	12.3–23.7
4	25	27.8315	14.4–27.6
5	30	33.387	16.4–31.6
6	35	37.4516	17.8–34.2
7	40	39.01	18.5–35.5

The error was calculated in each of the seven payloads; cases 1 to 4 exhibit less than 1%, and the last three no more than 10%, averaging a total error of 3.4%, which is an acceptable value to proceed with the analysis of the cases; from the data of Table 3 and by applying the general equation of error percent it is possible to estimate the error per case.

$$\%error = \left(\frac{analysis\ result - experimental\ value}{analysis\ result} \right) * 100$$

In each case, the error was calculated for each of the seven references: case 1 = 0%; case 2 = 0%; case 3 = 0%; case 4 = 0.83%; case 5 = 5.35%; case 6 = 8.68%; case 7 = 8.97%. Applying an average to the above percentage error results in a $\%error$ = 3.40%. Figure 7 shows the comparative values from Table 3; age-related health conditions and the solution method (numerical or experimental) contribute to the difference between each curve displayed in the graph. However, there is an approximation between outcomes.

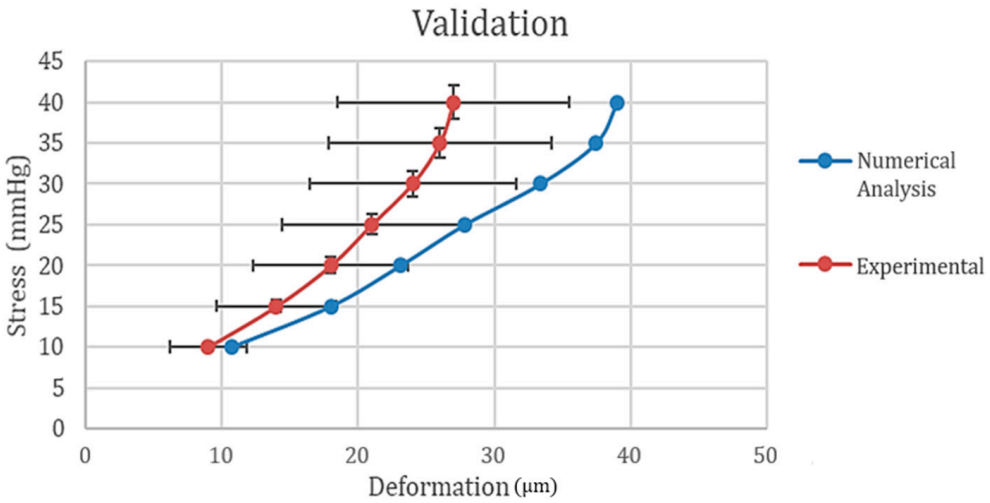

Figure 7. Stress–deformation curve, experimental and numerical results, own source.

The analysis of the cases to be studied was based on the procedure applied in the validation, but in this case, the whole model was contemplated for greater assertiveness in the results; thus, we were able to consider a more significant number of decimal places in the calculations. Also, the complete model (corneal surface) in the program, its exportation to STL, the tetrahedral mesh's application, and the assignation of the boundary conditions were used and configured. Figure 8 shows the free-body diagram into 2 views; (a) 3D view and (b) wireframe view.

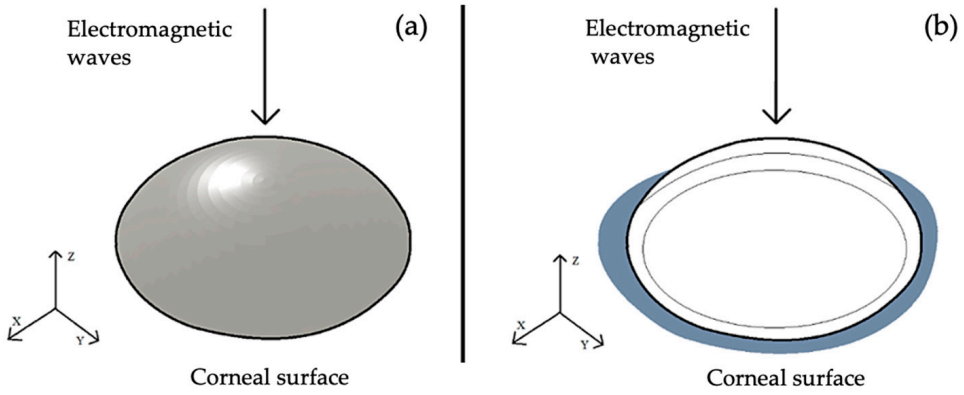

Figure 8. Study case, luminous beams on the surface's corneal eyeball.

Different justified restrictions were considered for each case, resembling, to a greater extent, the real condition that a human cornea presents when receiving a light beam. The base, which represents a direct restriction in the "Z" axis due to its union with the rest of the human organ, is the only restriction that concerns it, mainly because the light beam impacts from the "Z" axis. The inner side has restrictions in the "Y" and "X" axes. These restrictions are essential because represent the material's resistance, not losing its elliptical shape. Finally, the outer face, being the face to be deformed, does not have any constraint; as shown in Figure 9, the conditions were applied to develop the analysis.

Table 4 shows the power values consulted for different sources. In cases 3, 4, and 5, these values were obtained from user manuals and information from the sources. However, in the sun source, sunlight provides illumination of approximately 10,000 candelas/m^2 on a cloudy day and 50,000 candelas/m^2 on an ordinary day [32].

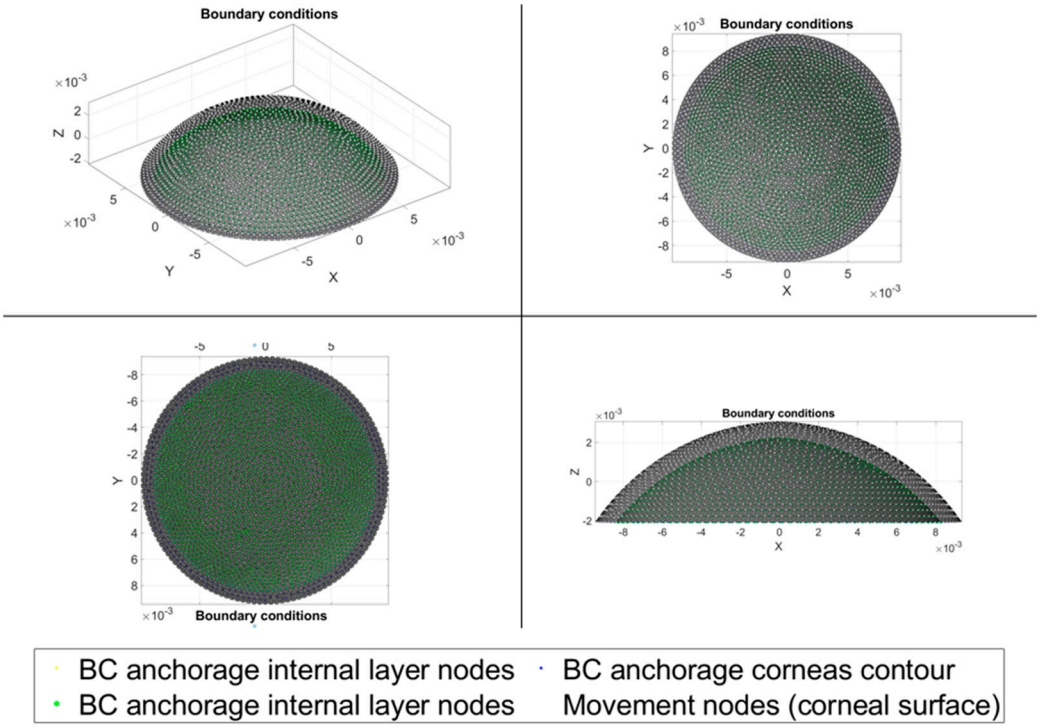

Figure 9. Node selection boundary conditions.

Table 4. Power values per case.

Case	Power [W]	Source	Distance (mm)	Photon Load (Pa)	Photons	Total Load Applied (Pa)
1	0.1	Sun	200	6.966×10^{-15}	15.106×10^{16}	1052.2616
2	0.0857	Sun	200	5.99×10^{-15}	15.106×10^{16}	905.8763
3	0.5	Smartphone's screen	200	4.5439×10^{-15}	157.85×10^{16}	7172.637
4	0.01	Commercial laser	200	2.09022×10^{-15}	5.0474×10^{16}	105.22616
5	1	Commercial laser	200	1.3934×10^{-15}	755.12×10^{16}	10,522.62

Five different results were obtained by using the values of Table 4; therefore, the outcomes show the results of the displacements. Once the values of all the cases have been obtained, it is possible to compare the load applied in each case and the displacements considering the boundary conditions.

4. Discussion

When comparing the results obtained numerically, there is a variance in the values obtained experimentally in the research contemplated. The outcomes in the validation are considered to have an absolute error of 3.2%. This error may be due to the patient's age, the dimensions of the parts of the visual organ, and the mechanical properties. The age of the subject for this research was a 72-year patient. Therefore, the variance in the graph is considered; due to age-related health conditions, there were significant deformations generated. The graph retains its characteristic curved shape, validating that the model and the analysis proposed employing the characteristic equation of the Ogden model satisfy the characteristic curve for viscoelastic materials. The values obtained in the five cases are presented in Table 5 to compare them.

Table 5. Summary results.

Case No.	Source (W)	Photon Load (Pa)	Photons Number	Total Load (Pa)	Maximum Displacement (μm)
1	0.1	6.966×10^{-15}	15.106×10^{16}	1052.2616	1.33
2	0.0857	5.99×10^{-15}	15.106×10^{16}	905.8763	1.14
3	0.5	4.5439×10^{-15}	157.85×10^{16}	7172.637	9.07
4	0.01	2.09022×10^{-15}	5.0474×10^{16}	105.22616	0.0837
5	1	1.3934×10^{-15}	755.12×10^{16}	10,522.62	13.3

Initially, we have the decrease in charge that an individual photon can generate. This is due to the different wavelength levels; the more influential the wavelength, the less charge it causes. This can be seen in cases 1 and 2; although the numbers of photons are the same, the total incident charge and the displacements decrease.

Specifically, case 3 is considered, for a screen of a smartphone at the minimum brightness of 200 mm; the generated charge is relatively high, and if the maximum brightness is considered, which is 1.5 W, it is estimated that the deformations increase. Because of this, it is possible to define the loads generated by luminous devices due to the amount of energy used to display clear and sharp images; therefore, it causes significant amounts of loads that are not lethal but can generate a constant load. Inconsequential fatigue failures due to repeated loads of non-infectious injuries, such as exposure to brightness over long periods, can cause damage to the eyeball, specifically on the corneal surface, causing eye diseases and blindness [33]. On the other hand, cases 4 and 5, which are commercial infrared lasers, show the importance of the electrical power by which the light source is supplied, because greater watt consumption by the source produces more photons and is directly proportional to the amount of load. Finally, the charge a photon generates depends on the electromagnetic spectrum to which it belongs. The direction a photon can generate is inversely proportional to its wavelength features. The analysis specifies that the deformations in the elastic region were due to the incident charges. Each case has a different result depending on the wave size and the power of the source. These case studies could even be extrapolated to cases where the cornea is subjected to extreme loads, such as refractive surgery, using a laser with specific characteristics, or proposing a photorefractive keratectomy (PRK). Alternatively, a current technique called Laser-Assisted in Situ Keratomileusis (LASIK) uses an ultraviolet laser. According to their datasheets, Table 6 shows the types of wavelengths for both cases.

Table 6. Overview of two eyeball surgery methods.

Surgeries Type	Applied Energy	Exposure Time	Wave Frequency	Area	Distance	Power
LASIK	2.5 μJ	350 fs	300 GHz	50.6 μm	150 mm	0.5 MW
PRK	2.5 μJ	350 fs	30 PHz	7.06 pm	150 mm	0.5 GW

This information is compiled from the information offered by different surgical devices, such as the Femto LDV Z8 Laser, and from manuals used for an operation, indications, and techniques. For example, consider the excimer laser type for LASIK surgery and Neodino for PRK. Due to the kind of surgery, PRK performs the load on a specific point of the cornea, whereas LASIK is applied over the entire corneal area.

Considering both specific cases where ablation occurs through scaling and the information collected, the amounts of load for each case are as follows:

- LASIK: 5×10^{10} Pa
- PRK: 7×10^{20} Pa

Both are the maximum cases to which a cornea can be subjected in this type of surgery.

5. Conclusions

In this research, a numerical simulation characterizes the structural deformations of the corneal surface by the irradiance of different luminous levels. The proposed hypothesis states that the light exerts mechanical stress (compressive stress) on the corneal surface, taking into consideration the power and wavelengths of luminous beams and the mechanical properties of the human eyeball; those loads can generate partial deformations due to overexposure in specific periods. By using open-source code programs that apply the FEM, it was possible to develop a whole numerical scenario based on our own pseudo coding, considering mechanical properties, mathematical models, and the study case to analyze the behavior of the corneal surface under different loads. This method and the numerical simulation based on the C program language can be used for different structural static analyses of biological tissues from the human body. Outcomes show the structural displacements under the irradiation of light depending on the brightness, the distance, and the wavelength; common devices such as screens of smartphones show maximum displacements up to 9.07 μm when the blue light of the screen is at 200 mm. On the other hand, it is important to consider the concentration of laser beams on surfaces; optical tweezers produce radiation of pressure which in nanometric and micrometric scales produces forces of light moving the particles of the irradiated surface. The cornea is the transparent structure through which the human organ filters and refracts the light. Therefore, a slight change in the cornea geometry significantly affects the optical tissue. In a viscoelastic material, these deformations totally disappear; however, because the cornea tends to thin with age, these effects grow exponentially, leading to pathogenesis or diseases in older people.

Author Contributions: Conceptualization, F.G.-L. and C.R.T.-S.; methodology, C.R.T.-S.; software, F.G.-L.; validation, J.A.F.-C., J.L.T.-A. and E.A.A.-A.; formal analysis, M.A.G.-C. and C.R.T.-S.; investigation, C.R.T.-S.; resources, M.A.G.-C.; data curation, F.G.-L. and J.L.T.-A.; writing—original draft preparation, F.G.-L. and J.A.F.-C.; writing—review and editing, C.R.T.-S.; visualization, M.A.G.-C.; supervision; project administration, E.A.A.-A.; funding acquisition, C.R.T.-S. All authors have read and agreed to the published version of the manuscript.

Funding: The authors are thankful to the Consejo Nacional de Humanidades, Ciencia y Tecnología (CONAHCyT), and the Instituto Politécnico Nacional for the support received in SIP 20231625 and SIP 20231131, as well as the EDI grant, all from SIP/IPN.

Institutional Review Board Statement: Not applicable.

Informed Consent Statement: Not applicable.

Data Availability Statement: Not applicable.

Acknowledgments: The authors are thankful to the Instituto Politécnico Nacional and an EDI grant from SIP/IPN.

Conflicts of Interest: The authors declare no conflict of interest.

References

1. Weisentha, R.W. *2014–2015 Basic and Clinical Science Course (BCSC): Section 8: External Disease and Cornea*; American Academy of Ophthalmology: San Francisco, CA, USA, 2014.
2. Nan, L.; Zhang, Y.; Song, H.; Ye, Y.; Jiang, Z.; Zhao, S. Influence of Light-Emitting Diode-Derived Blue Light Overexposure on Rat Ocular Surface. *J. Ophthalmol.* **2023**, *2023*, 1097704. [CrossRef]
3. Gulzar, A.; Yıldız, E.; Kaleli, H.N.; Nazeer, M.A.; Zibandeh, N.; Malik, A.N.; Taş, A.Y.; Lazoğlu, I.; Şahin, A.; Kizilel, S. Ruthenium-induced corneal collagen crosslinking under visible light. *Acta Biomater.* **2022**, *147*, 198–208. [CrossRef] [PubMed]
4. Liou, H.L.; Brennan, N.A. Anatomically accurate, finite model eye for optical modeling. *JOSA A* **1997**, *14*, 1684–1695. [CrossRef] [PubMed]
5. Feretis, E.; Theodorakopoulos, P.; Varotsos, C.; Efstathiou, M.; Tzanis, C.; Xirou, T. On the plausible association between environmental conditions and human eye damage. *Environ. Sci. Pollut. Res.* **2002**, *9*, 163–165. [CrossRef] [PubMed]
6. Ng, E.Y.K.; Ooi, E.H. FEM simulation of the eye structure with bioheat analysis. *Comput. Methods Programs Biomed.* **2005**, *82*, 268–276. [CrossRef] [PubMed]

7. Li, E.; Lui, G.T.; Tan, V.; He, Z.C. Modeling and simulation of bioheat transfer in the human eye using the 3D alpha finite element method. *Int. J. Numer. Methods Biomed. Eng.* **2010**, *26*, 955–976. [CrossRef]
8. Schaumburg, F.; Guarnieri, F.A. Simulación computacional de la interacción con el campo electromagnético del tejido adyacente un implante ocular. *Mecánica Comput.* **2012**, *16*, 3883–3898.
9. Álvarez, N.D.R.; Torres, C.S. Simulación y Modelamiento del ojo Humano como Herramienta Para la Prevención del Glaucoma a Través la Medición de la Presión Intraocular. Bachelor's Thesis, Universidad Politécnica Salesiana Sede Cuenca, Cuenca, Ecuador, 2015.
10. Esposito, L.; Clemente, C.; Bonora, N.; Rossi, T. Modelling human eye under blast loading. *Comput. Methods Biomech. Biomed. Eng.* **2015**, *18*, 107–115. [CrossRef]
11. Simonini, I.; Pandolfi, A. Customized finite element modelling of the human cornea. *PLoS ONE* **2015**, *10*, e0130426. [CrossRef]
12. Wang, X.; Rumpel, H.; Lim, W.E.H.; Baskaran, M.; Perera, S.A.; Nongpiur, M.E.; Girard, M.J. Finite element analysis predicts large optic nerve head strains during horizontal eye movements. *Investig. Ophthalmol. Vis. Sci.* **2015**, *57*, 2452–2462. [CrossRef]
13. Karimi, A.; Razaghi, R.; Navidbakhsh, M.; Sera, T.; Kudo, S. Computing the stresses and deformations of the human eye components due to a high explosive detonation using fluid–structure interaction model. *Injury* **2016**, *47*, 1042–1050. [CrossRef]
14. Karimi, A.; Razaghi, R.; Navidbakhsh, M.; Sera, T.; Kudo, S. Quantifying the injury of the human eye components due to tennis ball impact using a computational fluid–structure interaction model. *Sports Eng.* **2016**, *19*, 105–115. [CrossRef]
15. Whitford, C.; Joda, A.; Jones, S.; Bao, F.; Rama, P.; Elsheikh, A. Ex vivo testing of intact eye globes under inflation conditions to determine regional variation of mechanical stiffness. *Eye Vis.* **2016**, *3*, 21. [CrossRef]
16. Seven, I.; Vahdati, A.; Pedersen, I.B.; Vestergaard, A.; Hjortdal, J.; Roberts, C.J.; Dupps, W.J. Contralateral eye comparison of SMILE and flap-based corneal refractive surgery: Computational analysis of biomechanical impact. *J. Refract. Surg.* **2017**, *33*, 444–453. [CrossRef] [PubMed]
17. APant, D.; Kagemann, L.; Schuman, J.S.; Sigal, I.A.; Amini, R. An imaged-based inverse finite element method to determine in-vivo mechanical properties of the human trabecular meshwork. *J. Model. Ophthalmol.* **2017**, *1*, 100.
18. Prieto-Vázquez, A.Y.; Cuautle-Estrada, A.; Grave-Capistrán, M.A.; Ramírez, O.; Torres-SanMiguel, C.R. Fractal Analysis and FEM Assessment of Soft Tissue Affected by Fibrosis. *Fractal Fract.* **2023**, *7*, 661. [CrossRef]
19. Xu, M. Investigation of Corneal Biomechanical and Optical Behaviors by Developing Individualized Finite Element Model. Ph.D. Thesis, Mechanical Engineering, University of Rochester, Rochester, NY, USA, 2019.
20. Kumar, V.; Abbas, A.K.; Fausto, N.; Astar, J.C. *Patología Estructural y Funcional*, 8th ed.; Elsevier: Barcelona, Spain, 2013; Volume 53.
21. Bourne, R.R.A.; Flaxman, S.R.; Braithwaite, T.; Cicinelli, M.V.; Das, A.; Jonas, J.B. Magnitude, temporal trends, and projetions of the global prevalence of blindness and distance and near vision impairment: A systematic review and meta-analysis. *Lancet Glob. Health* **2018**, *5*, 3–10.
22. Vaughan, N. Evolution of Biological Eye in Computer Simulation. In Proceedings of the 2019 IEEE Congress on Evolutionary Computation(CEC), Wellington, New Zealand, 10–13 June 2019; pp. 2537–2543.
23. Andre, B.; Beckanhan, R.; Chou, B.R.; Gutstein, W.; Sliney, D.; Thomas, R.; Tsubota, K. ¿Qué papel debería jugar la ciencia y/o la práctica clínica en la prevención de los problemas oculares causados por los rayos ultravioletas y la luz azul violeta? *Points De Vue* **2014**, *71*, 8–9.
24. Ramirez, O.; Torres-San-Miguel, C.R.; Ceccarelli, M.; Urriolagoitia-Calderon, G. Experimental characterization of an osteosynthesis implant. In *Advances in Mechanism and Machine Science*; Uhl, T., Ed.; Springer: Berlin/Heidelberg, Germany, 2019; pp. 53–62.
25. Fada, R.; Shahgholi, M.; Azimi, R.; Babadi, N.F. Estimation of Porosity Effect on Mechanical Properties in Calcium Phosphate Cement Reinforced by Strontium Nitrate Nanoparticles: Fabrication and FEM Analysis. *Arab. J. Sci. Eng.* **2023**, *2023*, 1–11. [CrossRef]
26. León, M.G.; del Valle, A.; Elizondo, B.; Ortega, P.; Siller, M.F. Comparación de la becamedición del grosor corneal central medido con el paquímetro incluido en el Wavelight® Ex500 Excimer Laser y el tomógrafo de cámara de Scheimpflug Pentacam® en sujetos sanos. *Rev. Mex. De Oftalmol.* **2017**, *91*, 25–29.
27. Costanzo, L.S. *Fisiología*, 7th ed; Chapter 3; Neurofisiología—Fisiología; Elsevier: Amsterdam, The Netherlands; pp. 69–118. Available online: https://www-clinicalkey-com.bibliotecaipn.idm.oclc.org/student/content/book/3-s2.0-B9788413823812000039 (accessed on 13 January 2023).
28. Hamilton, K.E.; Pye, D.C. Young's modulus in normal corneas and the effect on applanation tonometry. *Optom. Vis. Sci.* **2008**, *85*, 445–450. [CrossRef] [PubMed]
29. Radiation Pressure, Wikipedia, The Free Encyclopedia, Year Last Revised 2022. Available online: https://en.wikipedia.org/wiki/Radiation_pressure (accessed on 24 August 2022).
30. Grytz, R.; Krishnan, K.; Whitley, R.; Libertiaux, V.; Sigal, I.A.; Girkin, C.A.; Crwford, J. A mesh-free approach to incorporate complex anisotropic and heterogeneous material properties into the eye-specific finite element models. *Comput. Methods Appl. Mech. Eng.* **2020**, *358*, 112654. [CrossRef]
31. Woo, S.L.; Kobayashi, A.S.; Schlegel, W.A.; Lawrence, C. Nonlinear material properties of intact cornea and sclera. *Exp. Eye Res.* **1972**, *14*, 29–39. [CrossRef] [PubMed]

32. Mark, N.; Farmer, K.C. *Sun Damage and Prevention*; Electronic Textbook of Dermatology; The Internet Dermatology Society, Inc.: New York, NY, USA, 2008.
33. Dang, D.H.; Riaz, K.M.; Karamichos, D. Treatment of Non-Infectious Corneal Injury: Review of Diagnostic Agents, Therapeutic Medications, and Future Targets. *Drugs* **2022**, *82*, 145–167. [CrossRef] [PubMed]